Harmonic dual dressing of spin-1/2 systems

Giuseppe Bevilacqua [●],[1,*] Valerio Biancalana [●],[1] T. Zanon-Willette [●],[2,3,4] and Ennio Arimondo[5,6]

[1]*Department of Physical Sciences, Earth and Environment – DSFTA, University of Siena, Italy*
[2]*Sorbonne Université, Observatoire de Paris, Université PSL, CNRS, LERMA, F-75005, Paris, France*
[3]*MajuLab, CNRS-UCA-SU-NUS-NTU International Joint Research Unit, Singapore*
[4]*Centre for Quantum Technologies, National University of Singapore, 117543 Singapore, Singapore*
[5]*Dipartimento di Fisica E. Fermi, Università di Pisa – Largo B. Pontecorvo 3, 56127 Pisa, Italy*
[6]*INO-CNR, Via G. Moruzzi 1, 56124 Pisa, Italy*

Controlled modifications of the magnetic response of a two-level system are produced in dressed systems by one high-frequency, strong, and nonresonant electromagnetic field. This quantum control is greatly enhanced and enriched by a harmonic, commensurable, and orthogonally oriented dual dressing, as discussed here. The secondary field enables a fine tuning of the qubit response, with control parameter amplitude, harmonic content, spatial orientation, and phase relation. Our analysis, mainly based on a perturbative approach with respect to the driving strength, includes also nonperturbative numerical solutions. The Zeeman response becomes anisotropic in a triaxial geometry and includes a nonlinear quadratic contribution. The long-time dynamics is described by an anisotropic effective magnetic field representing the handle for the system full engineering. Through the low-order harmonic mixing, the bichromatic driving generates a synthetic static field modifying the system dynamics. The spin temporal evolution includes a micromotion at harmonics of the driving frequency whose role in the spin detection is examined. Our dressing increases the two-level energy splitting, improving the spin detection sensitivity. In the weak-field direction it compensates the static fields applied in different geometries. The results presented here lay a foundation for additional applications to be harnessed in quantum simulations.

I. INTRODUCTION

Since the early days of quantum mechanics, spectroscopy probes the energy levels of quantum systems irradiated by electromagnetic fields. Single, bichromatic, multiple excitations are applied. More recently, those excitations target the modification and the control of quantum properties for the targeted object. Quantum variables, energies, and observables are manipulated. Within the quantum simulation effort, the electromagnetic driving of simple quantum systems (mainly natural or artificial atoms) generates Hamiltonians exhibiting interesting properties hard to engineer directly. Driving a quantum system periodically in time can profoundly alter its long-time dynamics and constitutes a versatile scenario to reach unusual quantum properties [1–3]. The dynamics associated with time-dependent Hamiltonians is well captured by time-independent effective Hamiltonians, accounting for the essential characteristics of the modulated system.

Within this area of Floquet engineering, a pioneering role is played by the "dressed atom" introduced by Cohen-Tannoudji and Haroche [4], i.e., the strong driving of a two-level quantum system. The application of a nonresonant and linearly polarized electromagnetic field, typically radio frequency or microwave, allows one to modify the magnetic response. The modifications of the Landé *g* factor were explored and applied in various atomic vapor experiments [5–13]. The

magnetic dressing was studied also with cold atoms and condensates [14–16]. It offers a powerful tool in quantum control experiments [17], high-resolution magnetometry [18], and spin-exchange relaxation experiments [19]. A key feature of this single dressing is the eigenenergy dependence on the J_0 (zero-order first kind Bessel function), allowing a freezing of the quantum observables. The close connection of this J_0 freezing with the tunneling suppression was pointed out in [20] and with the dynamical localization in optical lattice reviewed in [3].

A dual dressed qubit is examined here, more precisely, a two-level quantum system dressed by strong bichromatic harmonic drivings based on linearly polarized dressing fields applied along two orthogonal axes. Its theory and applications to different experimental configurations are presented. We compare our analyses to the previous single-dressing experiments and to the dual-dressing Cs atom experiment of Ref. [21] based on a weak secondary dressing. The dual-dressing quantum control is based on the combination of key ingredients as double irradiation by the harmonic bichromatic field, large interferences in the harmonic excitation processes, strong dressed-atom driving, and the generation of effective and synthetic fields controlling the spin dynamics. Even if each of these ingredients was examined previously, their combined action was not.

The bichromatic harmonic driving belongs to the general problem of periodically driven quantum systems, with pioneering contributions in [22,23]. Multifrequency excitation

---

*giuseppe.bevilacqua@unisi.it

has received much theoretical attention based on the continued fraction of matrices and complex numerical solutions [24–26]. Double irradiations, i.e., rotary saturation, spin tickling, and so on, are powerful tools in magnetic resonance to disentangle complex spectra. In [27] a low-order perturbation analysis of the Floquet treatment examines those regimes. Experiments in quantum optics have studied the bichromatic driving as reviewed in [28,29]. The attention was focused mainly on the absorption of atoms and molecules, and more recently, also of artificial atoms in [30–34]. Incommensurable dual driving is used by [35] for the evaporative cooling control, by [36,37] for the shield of optical clock transitions from magnetic static field, and for the probing of atom-photon interactions in [38].

The interference in the driving of a two-level system by several harmonic fields was examined in the magnetic resonance experiments of Refs. [39,40]. The dual modulation driving in an optical lattice clock by Ref. [41] evidences both the interference and the driving phase role.

The bichromatic harmonic excitation is important for the physics of ultracold atoms in optical lattices. The generated tunneling suppression in a lattice dual well, i.e., a generalization of the J_0 freezing, is examined theoretically in [42,43] and experimentally in [44]. That driving also allows the engineering of nearest-neighbor interactions in [45] and the dissipation processes in [46].

The dressed-atom modification by a second electromagnetic field with its frequency quasiresonant with the dressing one was briefly explored by Ref. [47] in 1983. An effective Hamiltonian is often used to analyze the dynamics of driven quantum systems [1–3]. Reference [43] derives such a Hamiltonian for a tight-binding model of the bichromatic driving. For the atomic trapping by rf dressed adiabatic potentials, that Hamiltonian describes the synthetic fields created by commensurable bichromatic or multiple drivings [48]. An effective Hamiltonian for the action of the bichromatic drive on a two-level system is introduced by [49]. As an equivalent of our synthetic field, the bichromatic harmonic driving produces a rectified transport when applied to external degrees of freedom, as for quantum ratchets in [50–52]. That effective Hamiltonian is examined by [53] in an experimental driving of ultracold atoms. The rectified transport is studied in [54] for a graphene model based on the coupling between driven spin and electron momentum.

Our analysis shows that a dressed spin experiences a micromotion, i.e., a temporal evolution, at harmonics of the driving frequency, as for other periodically driven quantum systems in [1]. From an experimental point of view, the micromotion has received much attention for trapped ions and for atoms in optical lattices by [55,56]. We derive that in single and dual spin dressing the micromotion is composed of two separate components, one given by a gauge transformation and the second one by a kick operator. Their role on the dressed evolution and detection is discussed.

Owing to the combination of the above ingredients, important original features are associated to this configuration. The eigenvectors and eigenvalues of the dressed spin are described by an effective magnetic Hamiltonian, providing a simple description of the spin dynamics. Its terms are finely tuned by the dressing amplitudes, their relative phase, the spatial orientation of the dressing fields, and the driving harmonic
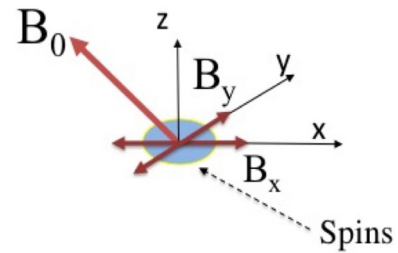

FIG. 1. Schematic of an atomic spin system dressed by the B_x and B_y oscillating fields in the presence of static field $\boldsymbol{B}_0$ arbitrarily oriented. Initially the spins are optically pumped into an eigenstate.

order. At weak static fields, the lowest order Zeeman coupling with the static field is described by an effective tensorial Landé g factor, with a triaxial magnetic control analog to the magnetic anisotropies appearing in solid-state materials. A weak tensorial nonlinear Zeeman coupling contributes to the effective Hamiltonian. The dual dressing creates an arbitrarily oriented synthetic static magnetic field, i.e., even in absence of a real external field. The underlying process, a nonlinear optical rectification of the dressing fields, is equivalent to light-shifts, even higher-order ones, due to the combined action of those fields. The effective Hamiltonian components are determined by the interferences between the absorption and emission processes of both fields, the interferences being enhanced by the low-harmonic order of the harmonic driving. These features introduce additional original degrees of freedom in the quantum control of the spin dynamics.

Several applications for quantum technologies are presented. For instance, our dressing geometry generates effective magnetic fields one thousand times larger than the externally applied static field, or produces an arbitrary compensation of external, arbitrarily oriented static fields, with a reduced sensitivity to the dressing parameters. Even if our analysis concentrates on a two-level system, the presence of external levels does not modify the listed features because the dressing is based on a nonresonant excitation. All these tools constitute an exceptional handle in a wide range of directions, from selective spectroscopic detection to quantum simulation and computation.

This paper is structured as follows. After introducing the Hamiltonian and the associated Floquet engineering, Sec. II presents the dual-dressing main features. Section III investigates the perturbation regime with one dressing field larger than both the static field and the secondary dressing field. Section IV discusses the connection between experimental detection and system dynamics, including the micromotion. Section V explores original applications allowed by the dual dressing. A final section concludes our work. Short Appendices report mathematical derivations.

II. HAMILTONIAN AND EFFECTIVE FIELDS

A. The Hamiltonian

We consider a spin-1/2 system (either real or artificial atom) interacting with static and oscillating magnetic fields, as schematized in Fig. 1 for an atomic physics setup. The

spin-field coupling is determined by the gyromagnetic ratio $\gamma = g\mu_B/\hbar$, with g the Landé factor and μ_B the Bohr magneton. The $\boldsymbol{B}_0$ static magnetic field has components B_{0j} on the $j = (x, y, z)$ axes. The spin is driven by two time-dependent and periodic fields oriented along the x and y axes, respectively, with B_i the maximum value and $s_i(t)$ the time dependence, where $(i = x, y)$. The Hamiltonian is

$$H = \frac{\gamma}{2}[\boldsymbol{B}_0 \cdot \boldsymbol{\sigma} + B_x\, s_x(t)\, \sigma_x + B_y\, s_y(t)\, \sigma_y], \qquad (1)$$

with σ the Pauli matrices. We concentrate on the following time dependencies:

$$s_x(t) = \cos(\omega t), \qquad s_y(t) = \cos(p\omega t + \Phi), \qquad (2)$$

with p an integer and Φ the phase difference of the harmonic fields. The role of the s_x initial phase is briefly analyzed within the detection section.

The angular frequency ω is taken as the frequency unit. We introduce the dimensionless time $\tau = \omega t$ and the dimensionless $\boldsymbol{\omega}_0 = \gamma \boldsymbol{B}_0/\omega$ and $\Omega_i = \gamma B_i/\omega$, the bare Larmor frequency and the Rabi frequencies, respectively. The $U(\tau)$ time evolution operator of the Hamiltonian results in

$$i\dot{U}(\tau) = \tfrac{1}{2}[\boldsymbol{\omega}_0 \cdot \boldsymbol{\sigma} + \Omega_x\, s_x(\tau)\, \sigma_x + \Omega_y\, s_y(\tau)\, \sigma_y]U(\tau), \quad (3)$$

and within this rewriting the spin-field coupling is described by an effective g-Landé factor equal to 1.

The Floquet theorem [1–3] allows us to write

$$U(\tau) = \mathcal{M}(\tau)e^{-i\Lambda\tau}, \qquad (4)$$

with $\mathcal{M}(0) = 1$ and $\mathcal{M}(\tau + 2\pi) = \mathcal{M}(\tau)$. The $\mathcal{M}$ operator describes the spin micromotion, and $e^{-i\Lambda\tau}$ represents the stroboscopic evolution operator. For single dressing the $\mathcal{M}$ operator was derived in [57] up to the fourth-order perturbation in the dressing amplitude.

B. Effective field

The spin dynamics is determined by the Λ time-independent Floquet Hamiltonian. This matrix is not unique, since for a given U operator one can subtract multiples of the ω frequency from its diagonal elements and compensate by multiplying $\mathcal{M}(\tau)$ with a diagonal matrix. The Λ matrix is written as

$$\Lambda = \tfrac{1}{2}\boldsymbol{h} \cdot \boldsymbol{\sigma}, \qquad (5)$$

with its eigenvalues limited to the $[-1/2, 1/2]$ first Brillouin zone, as in Fig. 2 . The $\boldsymbol{h}$ vector, measured in energy units, represents an effective magnetic field. The $\lambda_{\pm}$ eigenvalues result:

$$\lambda_{\pm} = \pm\frac{\sqrt{\boldsymbol{h} \cdot \boldsymbol{h}}}{2}. \qquad (6)$$

The effective magnetic field produces an energy splitting described by the dressed Ω_L Larmor frequency given by

$$\Omega_L = \lambda_+ - \lambda_- = \sqrt{\boldsymbol{h} \cdot \boldsymbol{h}}. \qquad (7)$$

As in Fig. 2, the Larmor precession frequency may reach the maximum value of 1, or in natural units the ω value. Therefore at low ω_0 values Ω_L may become larger than the bare Larmor frequency, as in the figure.
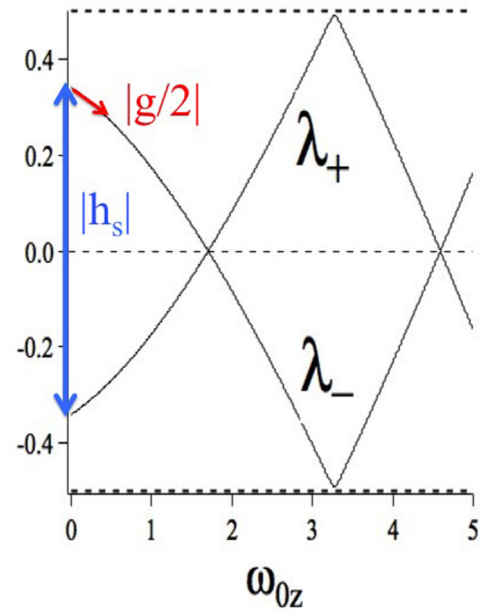
FIG. 2. First Brillouin zone λ_+, λ_- eigenvalues vs ω_{0z}. The $|\boldsymbol{h}_s|$ modulus is the energy separation at zero field. The $|\boldsymbol{g}|$ amplitude is the absolute value for the derivative of that separation. Parameters $\omega_{0x} = \omega_{0y} = 0$, $\Omega_x = 5.11$, $\Omega_y = 3$, $p = 1$, $\Phi = \pi/2$. For this case, at $\omega_0 \simeq 0$, $\Omega_L = \lambda_+ - \lambda_-$ is larger than ω_0.

The eigenstates of the Λ operator of Eq. (5) correspond to the spin oriented parallel or antiparallel to the $\boldsymbol{h}$ vector, i.e., the orientation unit vector $\boldsymbol{u} = \boldsymbol{h}/\Omega_L$. The spin precession takes place in the plane orthogonal to $\boldsymbol{u}$. The effective field definition may be rewritten as

$$\Lambda = \tfrac{1}{2}\,\Omega_L \boldsymbol{u} \cdot \boldsymbol{\sigma}. \qquad (8)$$

The effective field $\boldsymbol{h}$ depends on both $\boldsymbol{\omega}_0$ and Ω_i, with $(i = x, y)$. In the small $\boldsymbol{\omega}_0$ limit of our interest, we introduce the following Taylor expansion:

$$h_i(\boldsymbol{\omega}_0, \Omega_x, \Omega_y) = h_{s,i} + \sum_{j=x,y,z} \mathbf{g}_{ij}\, \omega_{0j}$$
$$+ \frac{1}{2} \sum_{j,k=x,y,z} \mathbf{f}_{ijk}\, \omega_{0j}\, \omega_{0k} + \cdots . \quad (9)$$

The (Ω_x, Ω_y) parameter dependence applies to all the right side quantities. A similar expansion of the Floquet eigenvalue at zero magnetic field was derived for the Bloch-Siegert shift in [58].

The zeroth-order vector $\boldsymbol{h}_s$ synthetic (or fictitious) field represents a static field acting on the spin also in absence of the externally applied static field. It is given by the $\lambda_+ - \lambda_-$ energy separation at $\boldsymbol{\omega}_0 = 0$, as shown in Fig. 2. The $\boldsymbol{h}_s$ field is equivalent to the light shifts [59] and to the generalized Bloch-Siegert shifts [29]. Here it contains high-order shifts due to the combined action of the harmonic driving fields. The synthetic field is generated by a nonlinear optical rectification process of the harmonic driving fields.

Within the Taylor expansion of Eq. (9), the first-order Jacobian matrix denoted as **g** is given by

$$\mathbf{g}_{ij} \equiv \left.\frac{\partial h_i}{\partial \omega_{0j}}\right|_{\boldsymbol{\omega}_0 = \mathbf{0}}. \tag{10}$$

This tensor produces a linear Zeeman effect and represents the generalization of the diagonal Landé g factor introduced by [7]. Its modulus is schematically represented in Fig. 2. The g factor as a second-order tensor appears in electron spin resonance in solids. There the tensor principal axes (tensor eigenstates) are determined by the local fields. Here the **g** principal axes define the basic spatial directions of the spin magnetic response. The Pv_i for $i = (1, 3)$ principal values (tensor eigenvalues) contain phases modifying the spin temporal evolution.

The Taylor expansion leads to the **f** second-order gradient tensor defined by

$$\mathbf{f}_{ijk} \equiv \left.\frac{\partial^2 h_i}{\partial \omega_{0j}\,\partial \omega_{0k}}\right|_{\boldsymbol{\omega}_0 = \mathbf{0}}. \tag{11}$$

This tensor corresponds to a nonlinear and anisotropic Zeeman effect. It is equivalent to the Hessian control for the spin response in [60] and in geophysics to the full gradient tensor of a magnetic field [61].

III. PERTURBATIVE AND NUMERICAL SOLUTIONS

A perturbative approach allows us to derive in Secs. III A and III B general analytical expressions for the above-defined quantities for generic s_x, s_y time dependencies. In the following sections we focus on the cosine driving and present plots for the values of the components for effective and synthetic fields, **g** and **f** tensors. In that context the results of numerical solutions for the dual-dressing Hamiltonian are also presented.

A. Frequency-modulated rotating field

The case $\Omega_x \gg \Omega_y$ is considered here, always in the limit of a weak $\boldsymbol{\omega}_0$ static field. The opposite case would just correspond to swapping the axis labels. We define the x phase accumulated by the spin for a periodic $s_x(\tau)$ driving, more general than in Eq. (2):

$$\varphi_x(\tau) = \Omega_x \int_0^\tau s_x(\tau')d\tau'. \tag{12}$$

For a rotating dressing field the interaction representation in a frame rotating about the static field axis simplifies the description. For our case of weak static fields such a usual rotating wave approximation is not valid. Therefore we introduce an interaction representation with respect to the strong Ω_x dressing field, the time evolution operator being factorized as

$$U(\tau) = e^{-i\varphi_x \sigma_x/2}\, U_I(\tau). \tag{13}$$

This gauge transformation represents a unitary change to a reference frame rotating about the x axis with a rotation angle presenting a nontrivial time dependence. For the s_x sinusoidal time dependence, the rotation angle experiences a frequency-modulated rotation (FMR), as denoted in [62].

The U_I time evolution is given by

$$i\dot{U}_I(\tau) = \tfrac{1}{2}e^{i\varphi_x \sigma_x/2}[\boldsymbol{\omega}_0 \cdot \boldsymbol{\sigma} + \Omega_y s_y(\tau)\sigma_y]e^{-i\varphi_x \sigma_x/2}\, U_I(\tau). \tag{14}$$

We apply the explicit expression for the exponentials of Pauli matrices, use the Baker-Campbell-Hausdorff relation, and manipulate the result with the commutation rules of those matrices. After this algebra the U_I operator is rewritten as

$$i\dot{U}_I(\tau) = \tfrac{1}{2}[\boldsymbol{h}^{\mathrm{FMR}}(\tau) \cdot \boldsymbol{\sigma}]\, U_I(\tau), \tag{15}$$

with $\boldsymbol{h}^{\mathrm{FMR}}(\tau)$ given by

$$\boldsymbol{h}^{\mathrm{FMR}}(\tau)$$
$$= \begin{pmatrix} \omega_{0x} \\ \omega_{0y}\cos(\varphi_x(\tau)) + \omega_{0z}\sin(\varphi_x(\tau)) + \Omega_y s_y(\tau)\cos(\varphi_x(\tau)) \\ \omega_{0z}\cos(\varphi_x(\tau)) - \omega_{0y}\sin(\varphi_x(\tau)) - \Omega_y s_y(\tau)\sin(\varphi_x(\tau)) \end{pmatrix}. \tag{16}$$

The vector $\boldsymbol{h}^{\mathrm{FMR}}(\tau)$ represents the time-dependent field acting on the spin in the FMR reference frame. Because both the $s_x(\tau)$ signal of Eq. (2) and the $\varphi_x(\tau)$ are periodic functions, also the $\boldsymbol{h}^{\mathrm{FMR}}$ vector is periodic.

The time evolution of Eq. (15) being periodic, the Floquet theorem allows us to write the $U_I(\tau)$ operator as

$$U_I(\tau) = e^{-i\mathcal{K}(\tau)}\, e^{-i\Lambda\,\tau}, \tag{17}$$

where the kick operator $\mathcal{K}(\tau)$ is defined as in the modulated optical lattice descriptions [1–3]. The FMR kick operator is periodic and satisfies $\mathcal{K}(0) = 0$. Because the $U(\tau)$ laboratory frame operator is derived from the $U_I(\tau)$ FMR frame operator using Eq. (13), the Λ matrix of Eq. (17) is the stroboscopic operator introduced in Eq. (4).

B. First- and second-order solutions

The $U_I(\tau)$ evolution in the FMR frame allows us to derive from the time-dependent $\boldsymbol{h}^{\mathrm{FMR}}(\tau)$ of Eq. (16) an analytical expression of the effective static field $\boldsymbol{h}$ defined in Eq. (5), always in the limit of both Ω_y and $\boldsymbol{\omega}_0$ small parameters. From appropriate time averages of $\boldsymbol{h}^{\mathrm{FMR}}(\tau)$ of Appendix D, we derive the first- and second-order perturbation $\boldsymbol{h}$ expressions, defined as

$$\boldsymbol{h} \approx \boldsymbol{h}^{(1)} + \boldsymbol{h}^{(2)}. \tag{18}$$

Using Eq. (D9), the first order, given by the $\boldsymbol{h}^{\mathrm{FMR}}(\tau)$ FMR time average, results in

$$\boldsymbol{h}^{(1)} = \begin{pmatrix} \omega_{0x} \\ \omega_{0y}\langle\cos\varphi_x\rangle + \omega_{0z}\langle\sin\varphi_x\rangle + \Omega_y\langle s_y\cos\varphi_x\rangle \\ \omega_{0z}\langle\cos\varphi_x\rangle - \omega_{0y}\langle\sin\varphi_x\rangle - \Omega_y\langle s_y\sin\varphi_x\rangle \end{pmatrix}. \tag{19}$$

Using the α_n and β_n definitions in Appendix Eqs. (C1), we obtain the following first-order synthetic field and g tensor:

$$\boldsymbol{h}_s^{(1)} = \Omega_y \begin{pmatrix} 0 \\ \mathrm{Re}(\beta_0) \\ -\mathrm{Im}(\beta_0) \end{pmatrix}, \tag{20a}$$

$$\mathbf{g}^{(1)} = \begin{pmatrix} 1 & 0 & 0 \\ 0 & \mathrm{Re}(\alpha_0) & \mathrm{Im}(\alpha_0) \\ 0 & -\mathrm{Im}(\alpha_0) & \mathrm{Re}(\alpha_0) \end{pmatrix}$$

$$= \begin{pmatrix} 1 & 0 & 0 \\ 0 & |\alpha_0| & 0 \\ 0 & 0 & |\alpha_0| \end{pmatrix} \begin{pmatrix} 1 & 0 & 0 \\ 0 & \cos(\eta_0) & \sin(\eta_0) \\ 0 & -\sin(\eta_0) & \cos(\eta_0) \end{pmatrix},$$

(20b)

where $\tan \eta_0 = \mathrm{Im}(\alpha_0)/\mathrm{Re}(\alpha_0)$. At this order there is no contribution to $\mathbf{f}$.

This $\mathbf{g}^{(1)}$ expression represents a tensor nondiagonal and nonsymmetric, corresponding to a contraction and rotation of the spin response. Its Pv_i ($i = 1, 3$) principal values are $[1, \mathrm{Re}(\alpha_0) \pm i\mathrm{Im}(\alpha_0)]$. These complex conjugates ones correspond to tensor eigenvectors in the (y, z) plane experiencing a different phase shift with respect to the dressing fields.

The second-order synthetic field derived from Eq. (D10) contains a single component as

$$\boldsymbol{h}_s^{(2)} = \frac{\Omega_y^2}{2} \begin{pmatrix} Q_x \\ 0 \\ 0 \end{pmatrix},$$

(21)

with

$$Q_x = \sum_{n \neq 0} \frac{|\beta_n|^2 - 2\mathrm{Re}(\beta_0^* \beta_n)}{n}.$$

(22)

The second-order expression of the g tensor reads as

$$\mathbf{g}^{(2)} = \frac{\Omega_y}{2} \begin{pmatrix} 0 & Q_{xy} & Q_{xz} \\ Q_{yx} & 0 & 0 \\ Q_{zx} & 0 & 0 \end{pmatrix},$$

(23)

where

$$Q_{xy} = 2\mathrm{Re}\left(\sum_{n \neq 0} \frac{\beta_n \alpha_n^* - \beta_0 \alpha_n^* - \alpha_0^* \beta_n}{n} \right),$$

$$Q_{xz} = -2\mathrm{Im}\left(\sum_{n \neq 0} \frac{\beta_n \alpha_n^* - \beta_0 \alpha_n^* - \alpha_0^* \beta_n}{n} \right),$$

$$Q_{yx} = 2\mathrm{Re}\left(\sum_{n \neq 0} \frac{\beta_n}{n} \right),$$

$$Q_{zx} = -2\mathrm{Im}\left(\sum_{n \neq 0} \frac{\beta_n}{n} \right).$$

(24)

At this order the $\mathbf{f}_{i,j,k}^{(2)}$ tensor components, with $(i = x, y, z)$, are the following ones, respectively:

$$\left[\begin{pmatrix} 0 & 0 & 0 \\ 0 & q_0 & 0 \\ 0 & 0 & q_0 \end{pmatrix}, \begin{pmatrix} 0 & q_s & -q_c \\ q_s & 0 & 0 \\ -q_c & 0 & 0 \end{pmatrix}, \begin{pmatrix} 0 & q_c & q_s \\ q_c & 0 & 0 \\ q_s & 0 & 0 \end{pmatrix} \right],$$

(25)

where

$$q_0 = \sum_{n \neq 0} \frac{|\alpha_n|^2 - 2\mathrm{Re}(\alpha_n \alpha_0^*)}{n},$$

(26)

$$q_c = -\mathrm{Im}\left(\sum_{n \neq 0} \frac{\alpha_n}{n} \right),$$

(27)

$$q_s = \mathrm{Re}\left(\sum_{n \neq 0} \frac{\alpha_n}{n} \right).$$

(28)

At this order the $\mathbf{f}$ tensor components depend only on the strong-field variables, as for the $\mathbf{g}$ tensor at the first order.

C. Cosine signals

1. Phase-controlled cosines

The (x, y) cosine driving case of Eq. (2) with a controlled Φ phase difference between the driving fields is discussed here. The FMR accumulated phase of Eq. (12) becomes

$$\varphi_x(\tau) = \Omega_x \sin(\tau).$$

(29)

For the FMR accumulated phase of Eq. (12), using Eqs. (C6) the α_n functions appearing above reduce to the $J_n(\Omega_x)$ first-order Bessel functions and the β_n functions to combinations of those functions.

At the first-order perturbation, the synthetic field becomes

$$\boldsymbol{h}_s^{(1)} = \Omega_y J_p(\Omega_x) \begin{pmatrix} 0 \\ \cos(\Phi)\frac{1+(-1)^p}{2} \\ \sin(\Phi)\frac{1-(-1)^p}{2} \end{pmatrix}.$$

(30)

For the p-odd case, the z component only is different from zero, while for p even this applies to the y component. Figure 3(a) reports the Ω_x dependencies for the $p = 1$ $h_{s,z}^{(1)}$ and $p = 2$ $h_{s,y}^{(1)}$ components. The sign changes produced the Bessel functions are verified in the Cs experiment of [21].

The Q_x amplitude of the second-order synthetic field $\boldsymbol{h}_{s,x}^{(2)}$ component of Eq. (21) is derived in Eq. (E1) for the cosine drivings and plotted vs Ω_x for $(p = 1, 2)$ in Fig. 3(b). This second-order contribution is ten times weaker than the first-order contributions.

Outside the perturbation regime, the numerical analyses for $p = 1$ produce the h_z effective values of the Fig. 3(c) two-dimensional (2D) (Ω_x, Ω_y) plot. That figure evidences the periodic structures in the spin dynamic response to the dual dressing. In this strong regime the h_x value is comparable to h_z, while h_y remains identically zero.

The first-order g tensor results

$$\mathbf{g}^{(1)} = \begin{pmatrix} 1 & 0 & 0 \\ 0 & J_0(\Omega_x) & 0 \\ 0 & 0 & J_0(\Omega_x) \end{pmatrix}.$$

(31)

This diagonal $\mathbf{g}^{(1)}$, as in the original single-dressing treatment of Ref. [7], denotes that the tensor principal axes are parallel to the coordinate axes. Numerical results for J_0 Bessel dependence of the $\mathbf{g}^{(1)}$ on Ω_x are shown in Fig. 4(a).

The α_n and β_n dependencies on the Bessel functions of Eq. (E2) determine the Q_{ij} amplitudes of the $\mathbf{g}^{(2)}$ tensor components of Eq. (23). For the $p = 1$ harmonic the four components different from zero are plotted vs Ω_x in Fig. 4(b), all of them ten times weaker than the first order. The plots evidence the nonsymmetric form of the tensor. The $\mathbf{g}^{(1)} + \mathbf{g}^{(2)}$ tensor three principal values are either all real or one real and two complex conjugates, as presented in Fig. 4(c). While for $(p = 1, \Phi = 0)$ the three values are all real, the (Ω_x, Ω_y)
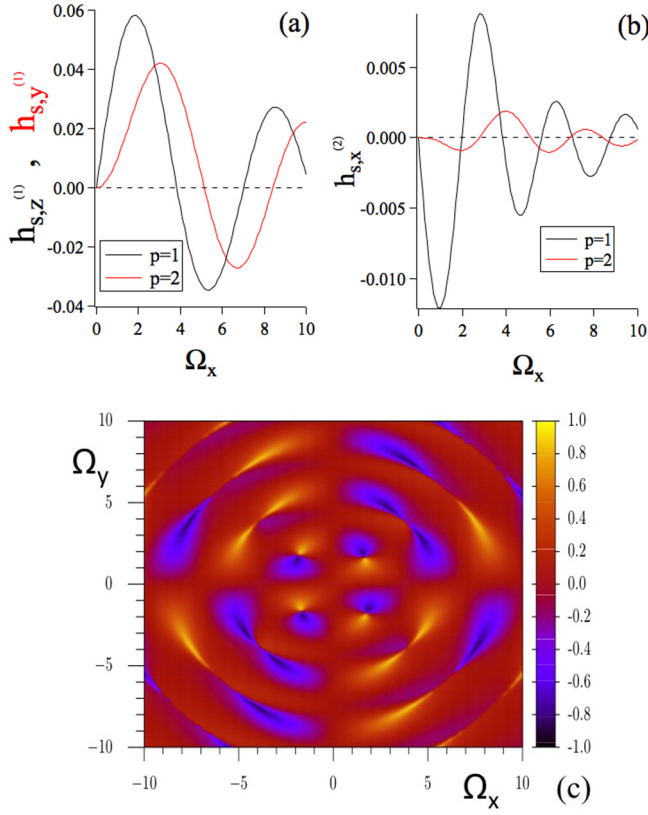
FIG. 3. Cosine driving synthetic and effective fields for $\omega_{0z} = 0.1$ and $\omega_{0x} = \omega_{0y} = 0$. In (a) and (b) synthetic fields derived from the perturbation treatment vs Ω_x at $\Omega_y = 0.1$. In (a) black line for $h_{s,z}^{(1)}$ at $p = 1$ and $\Phi = \pi/2$; red line $h_{s,y}^{(1)}$ at $p = 2$ and $\Phi = \pi/6$. In (b) second-order $h_{s,x}^{(2)}$ vs Ω_x at $\Omega_y = 0.2$ and $(p = 1, 2)$. In (c) numerical results for the h_z effective field in a (Ω_x, Ω_y) two-dimensional (2D) plot at $p = 1$ and $\Phi = \pi/2$.

region of complex values increases with Φ. For $(p = 1, \Phi = \pi/2)$ the regions with two complex values are denoted in red in the 2D plot of Fig. 4(c). Notice that from a physical point of view, the spin response should be symmetric by swapping Ω_x and Ω_y. This symmetry does not appear in the Fig. 4(c) plot, because for each ϕ phase the gauge transformation to the FMR reference frame leads to a different eigenvalue phase shift.

Figure 5 reports the q_0 and q_s quantities of $\mathbf{f}^{(2)}$ components as derived in Eqs. (E4), q_c being equal zero. At this perturbation level no dependence on Ω_y is present. The nonlinear Zeeman contribution to the effective field assumes a maximum value $\approx 0.5(\omega_{0y}^2 + \omega_{0z}^2)$ for both diagonal and nondiagonal components of the tensor.

2. Shifted cosine driving

In order to present the role played by the initial phase ψ within the FMR gauge transformation. We examine the case of the dual dressing with

$$s_x(\tau) = \cos(\tau + \psi),$$
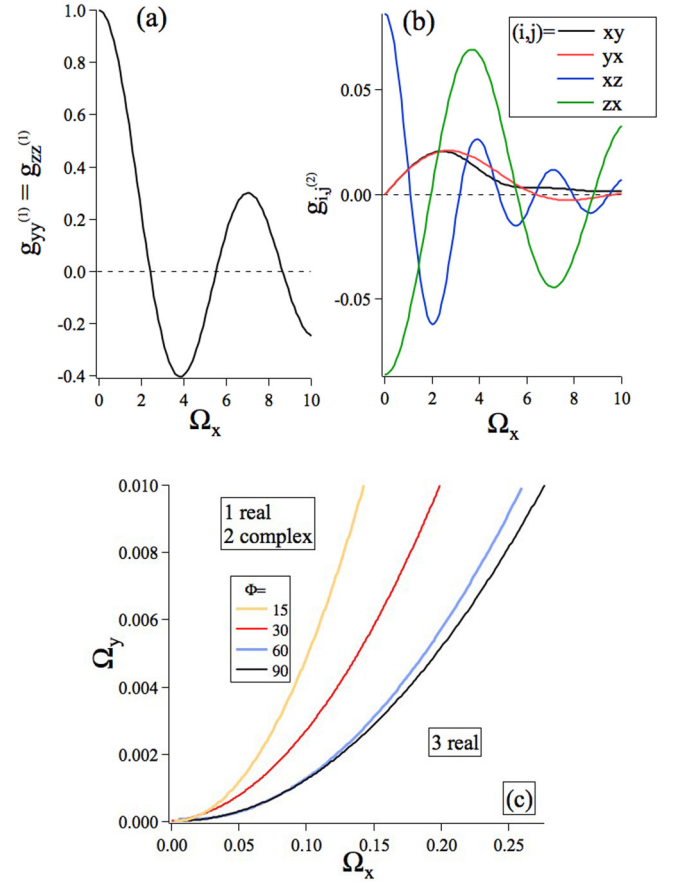$$s_y(\tau) = \cos[(p\tau + \psi) + \Phi], \tag{32}$$

FIG. 4. Cosine driving results for the **g** components. In (a) $\mathbf{g}_{xx}^{(1)} = \mathbf{g}_{yy}^{(1)}$ components vs Ω_x, given by the J_0 Bessel function and independent of Ω_y. In (b) $\mathbf{g}_{ij}^{(2)}$ tensor components vs Ω_x at $\Omega_y = 0.2$, $p = 1$, and $\Phi = \pi/3$. In (c) perturbation-derived lines separating the (Ω_x, Ω_y) regions of real principal values, below the parabole, and of real or complex principal values, above the parabole. Parameters $p = 1$ and different Φ values.
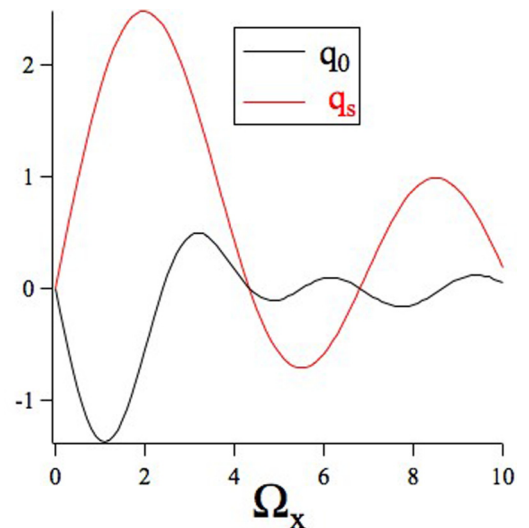

FIG. 5. Results for the q_0 and q_s functions determining the $\mathbf{f}^{(2)}$ tensor components vs Ω_x. They are independent of the Ω_y parameter.

with Φ again the relative phase between the drivings. An equivalent role of the initial phase occurs for the Floquet gauges of periodically driven optical lattices [63]. In addition, the $\Omega_y = 0$ case with the ψ phase not properly controlled describes all the single-dressing atom experiments of Refs. [5–8,10–13,16].

The first-order synthetic field is given by Eq. (20) with the following β_0 expression:

$$
\beta_0 = \begin{cases} J_p(\Omega_x) \cos(p\psi - \Phi) e^{-i\xi \sin(\psi)} & p \text{ even} \\ iJ_p(\Omega_x) \sin(p\psi - \Phi) e^{-i\xi \sin(\psi)} & p \text{ odd} \end{cases}. \quad (33)
$$

For the $\mathbf{g}^{(1)}$ tensor we obtain

$$
\mathbf{g}^{(1)} = \begin{pmatrix} 1 & 0 & 0 \\ 0 & J_0(\Omega_x) & 0 \\ 0 & 0 & J_0(\Omega_x) \end{pmatrix} \begin{pmatrix} 1 & 0 & 0 \\ 0 & \cos(\tilde{\Psi}) & -\sin(\tilde{\Psi}) \\ 0 & \sin(\tilde{\Psi}) & \cos(\tilde{\Psi}) \end{pmatrix}, \quad (34)
$$

where $\tilde{\Psi} = \Omega_x \sin(\psi)$, and the tensor is written as the product of a contraction and a rotation. The nondiagonal matrix elements depending on the ψ parameter lead to complex principal values corresponding to phase rotations in the plane orthogonal to the single-dressing field. As presented in the following section, the ψ phase modifies the detected spin evolution.

IV. SPIN EVOLUTION AND DETECTION

A. Micromotion

The dressing operation modifies mean value and time evolution of the spin components. These quantities are derived from the $U(\tau)$ time evolution operator of Eq. (13) rewritten using Eq. (17) as

$$
U(\tau) = e^{-i\varphi_x \sigma_x/2} e^{-i\mathcal{K}(\tau)} e^{-i\Lambda \tau}, \quad (35)
$$

leading to the micromotion operator in the laboratory frame

$$
\mathcal{M}(\tau) = e^{-i\varphi_x(\tau)\sigma_x/2} e^{-i\mathcal{K}(\tau)}. \quad (36)
$$

The $\mathcal{K}$ kick operator, as derived at the first-order perturbation in Appendix F, is the sum of two terms, one proportional to $\boldsymbol{\omega}_0$ and the other to Ω_y. Therefore for all the single- and dual-dressing experiments performed so far with low values for those fields, the spin micromotion of Eq. (36) is dominated by the first term determined by the transformation to the FMR frame.

B. Expectation values

Using the Pauli matrix exponentiation and the effective field Λ expression of Eq. (8), the $\sigma_x(\tau)$ operator becomes

$$
\sigma_x(\tau) = U(\tau)^\dagger \sigma_x(0) U(\tau) \approx \left[\left(1 - u_x^2\right) \cos \Omega_L \tau + u_x^2 \right] \sigma_x(0)
$$
$$
+ [u_x u_y (1 - \cos \Omega_L \tau) - u_z \sin \Omega_L \tau] \sigma_y(0)
$$
$$
+ [u_x u_z (1 - \cos \Omega_L \tau) + u_y \sin \Omega_L \tau] \sigma_z(0), \quad (37)
$$

where the kick operator contribution is neglected. A similar algebra derives the $\sigma_y(\tau)$ and $\sigma_z(\tau)$ evolutions. For an initial $\langle \sigma_x(0) \rangle = 1$ eigenstate, the spin expectation values, measured by the absorption or dispersion of lasers propagating along the

Fig. 1 axis, are

$$
\langle \sigma_x(\tau) \rangle = \left(1 - u_x^2\right) \cos(\Omega_L \tau) + u_x^2,
$$
$$
\langle \sigma_y(\tau) \rangle = [u_y \sin \varphi_x + u_z \cos \varphi_x] \sin(\Omega_L \tau)
$$
$$
+ [u_x u_y \cos \varphi_x - u_x u_z \sin \varphi_x](1 - \cos(\Omega_L \tau)),
$$
$$
\langle \sigma_z(\tau) \rangle = [u_z \sin \varphi_x - u_y \cos \varphi_x] \sin(\Omega_L \tau)
$$
$$
+ [u_x u_z \cos \varphi_x + u_x u_y \sin \varphi_x](1 - \cos(\Omega_L \tau)), \quad (38)
$$

where $\varphi_x(\tau)$ is given by Eq. (29). These expressions generalize the derivation in Ref. [9]. The spin coherences contain two separate time dependencies, the Ω_L frequency precession, and a more complex micromotion one determined by the $\cos(\varphi_x(\tau))$ and $\sin(\varphi_x(\tau))$ functions at the harmonics of the driving frequency.

C. Detection in shifted cosine single dressing

The spin detection in the pioneer single-dressing experiment by Landré *et al.* [7] highlights the role of the off-diagonal elements in the $\mathbf{g}$ tensor of Eq. (34). No phase control is applied to the dressing field, and that experiment is described by the shifted single cosine treatment of Sec. III C 2 with $\Omega_y = 0$. With the $\langle \sigma_x(0) \rangle = 1$ mercury atoms prepared initially, at $t = 0$ time a weak $\omega_{0y} \neq 0$ magnetic field is switched on. No synthetic field is created because $\Omega_y = 0$. The effective field $\boldsymbol{h}$ vector derived from Eq. (34) is

$$
\boldsymbol{h} = \begin{pmatrix} 0 \\ \omega_{0y} J_0(\Omega_x) \cos(\Omega_x \sin(\psi)) \\ \omega_{0y} J_0(\Omega_x) \sin(\Omega_x \sin(\psi)) \end{pmatrix}, \quad (39)
$$

leading to $\Omega_L = \omega_{0y}|J_0(\Omega_x)|$ and to the $\boldsymbol{u}$ orientation vector

$$
\boldsymbol{u} = \begin{pmatrix} 0 \\ \mathrm{sgn}(J_0) \cos(\Omega_x \sin(\psi)) \\ \mathrm{sgn}(J_0) \sin(\Omega_x \sin(\psi)) \end{pmatrix}, \quad (40)
$$

with no dependence on the static field. Using Eq. (C5) for dealing with the $\cos(\varphi_x(\tau))$ and $\sin(\varphi_x(\tau))$ of Eqs. (38), we obtain

$$
\langle \sigma_x(\tau) \rangle = \cos(\Omega_L \tau),
$$
$$
\langle \sigma_y(\tau) \rangle = \sin(\Omega_L \tau) \sin[\Omega_x \sin(\tau + \psi)]
$$
$$
= 2 \sin(\Omega_L \tau)[J_1 \sin(\tau + \psi)
$$
$$
+ J_3 \sin(3\tau + 3\psi) + \cdots],
$$
$$
\langle \sigma_z(\tau) \rangle = -\sin(\Omega_L \tau) \cos[\Omega_x \sin(\tau + \psi)]
$$
$$
= -\sin(\Omega_L \tau)[J_0 + 2J_2 \cos(2\tau + 2\psi) + \cdots]. \quad (41)
$$

The J_0 response in $\langle \sigma_z(\tau) \rangle$ is produced by the $\cos(\varphi_x(\tau))$ dependence, as pointed out in [16]. In the Landré *et al.* [7] experiment, the oscillations at the frequency Ω_L of the $\langle \sigma_x(\tau) \rangle$ and $\langle \sigma_z(\tau) \rangle$ spin components are detected by the probe beam propagating along those axes of Fig. 1. The xz plane spin evolution follows an ellipse contracted by $J_0(\Omega_x)$ on one axis. Within that Ω_L detection, the $\mathbf{g}$ tensor nondiagonal form of Eq. (34) does not play any role. In a detection sensitive to the sideband frequencies, the ψ dependence of the nondiagonal tensor terms, and also the micromotion contributions, can be detected. For an arbitrary static field orthogonal to
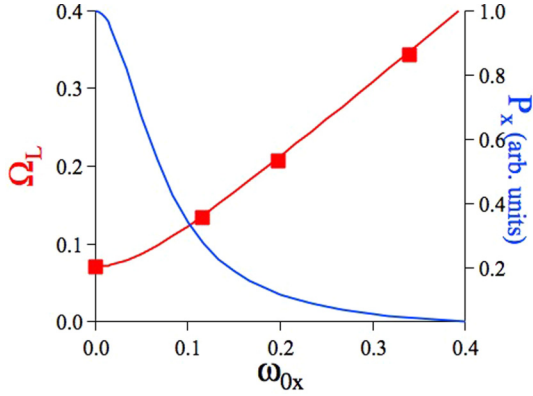
FIG. 6. The Ω_L Larmor frequency (left axis) and the P_{S_x} peak of the Ω_L oscillating Faraday signal peak (right axis) vs the applied ω_{0x} magnetic field measured in the Cs dual-dressing experiment [21]. Parameters: $\omega_{0z} = 0.1993(2)$, $\Omega_x = 1.833(5)$, $p = 1$, $\Omega_y = 0.0118(1)$, and $\Phi = \pi/2$.

the dressing x axis, an ellipse evolution takes place on the plane perpendicular to the static field. Such evolution matches the uniaxial cylindrical symmetry associated to the single dressing.

D. Detection in dual dressing

In Ref. [21] the dual dressing is tested for optically pumped Cs atoms. Because the detection is synchronized by the x dressing field and the Ω_x phase is fixed in the experiment, the system is described by the sinusoidal laws of Eq. (2). Optical pumping along the x axis and synchronous with the Ω_L precession frequency is applied to the spins. Faraday detection of a probe beam propagating along the x axis of Fig. 1 monitors the $\langle \sigma_x(\tau) \rangle$ time response at that frequency. Therefore the Ω_L dressed Larmor frequency and the P_x peak amplitude of a signal proportional to the Ω_L component of $\langle \sigma_x(\tau) \rangle$ are measured. We examine here the $p = 1$ dual-dressing detection at fixed values of (Ω_x, Ω_y) and ω_{0z} as a function of an ω_{0x} applied field. At the first perturbation order this field plays a dual role. It modifies Ω_L, given by

$$\Omega_L^{(1)}(\omega_{0x}) = \sqrt{\omega_{0x}^2 + [J_0(\Omega_x)\omega_{0z} + J_1(\Omega_x)\Omega_y \sin(\Phi)]^2}, \tag{42}$$

and the $\boldsymbol{u}$ spatial orientation, given by

$$\boldsymbol{u} = \frac{1}{\Omega_L^{(1)}} \begin{pmatrix} \omega_{0x} \\ 0 \\ J_0(\Omega_x)\omega_{0z} + J_1(\Omega_x)\Omega_y \sin(\Phi) \end{pmatrix}. \tag{43}$$

The Faraday detection signal monitors the following $\langle \sigma_x(\tau) \rangle$ derived from Eq. (38):

$$\langle \sigma_x(\tau) \rangle = A_x \cos(\Omega_L \tau) + \left(\frac{\omega_{0x}}{\Omega_L} \right)^2, \tag{44}$$

with A_x the oscillation amplitude,

$$A_x = \left[1 - \left(\frac{\omega_{0x}}{\Omega_L} \right)^2 \right]. \tag{45}$$

The measured Ω_L Larmor frequency and P_x value proportional to A_x are plotted in Fig. 6 vs the applied ω_{0x} field for the experimental parameters in the figure caption. The Ω_L dependence is well fitted by Eq. (42). The Lorentzian-shaped decrease of P_x with ω_{0x}, observed in the experiment but not carefully measured, is produced by the change in the spin precession plane orthogonal to the $\boldsymbol{u}$ orientation vector as modified by ω_{0x}. These results demonstrate the triaxial symmetry of the spin response. The micromotion does not appear on the experimental observed $\langle \sigma_x(t) \rangle$ signal. Equations (38) show that it can be monitored, detecting the orthogonal spin components.

V. DUAL-DRESSING APPLICATIONS

The control provided by the dual dressing leads to quantum technology advances in a variety of experimental configurations. Several ones are presented here, based on the flexible effective field tuning in amplitude and direction, for either one or two different spins.

A. Increased magnetic response

Because in magnetic resonance and other spectroscopic techniques the detection sensitivity increases with the spin precession frequency, it is important to increase, at a given real static magnetic field, the Ω_L Larmor frequency. This result, implemented by the dual dressing, is measured by the following $a\Omega_L$ accelerated Larmor frequency:

$$a\Omega_L = \frac{\Omega_L}{\omega_0}, \tag{46}$$

equal to 1 in the absence of the dressing. Owing to the periodic structure of the eigenfrequency Brillouin zones, the maximum allowed Ω_L value is 1. Therefore in the low-magnetic-field range of our interest $a\Omega_L$ becomes quite large. As shown in the numerical data of Fig. 7(a), for $p = 3$, $\omega_{0z} = 0.001$, and with a proper choice of the (Ω_x, Ω_y) values, $a\Omega_L$ reaches a maximum value of around 1000, as allowed by the Brillouin zone boundary. Such high frequency response leads to a very high sensitivity in the spin detection. Brillouin zone boundary ratios are reached for all the ω_{0z} values. A $p = 3$ perturbation treatment produces the $a\Omega_L$ of Fig. 7(b) with a maximum value at $\Phi = \pi/2$. The Φ phase dependence of the perturbation treatment applies also to the strong dressing regime. For each phase the maximum is obtained at different dressing parameters. Similar periodic maxima appear also for the $p = 1$, $\Omega_x = \Omega_y$, and $\Phi = \pm \pi/2$ rotating dressing case where the Larmor frequency is determined by the effective field in the rotating frame. They are originated by the folding of the dressed Larmor frequency into the periodic Brillouin structure.

In atomic interferometry experiments with a Stern-Gerlach deflection, a magnetic field gradient splits the particles into spatially separated paths, for instance, see Ref. [64]. The accelerated dressed Larmor frequency may be used to increase that deflection owing to the modified linear Zeeman splitting. This occurs when the bare Landé g factor, equal to 1 in our units, is replaced by a large principal value of the $\boldsymbol{g}$ tensor. Such a case is presented in Fig. 8 for the caption parameters. The absolute principal value of Pv_l (the largest one) increases
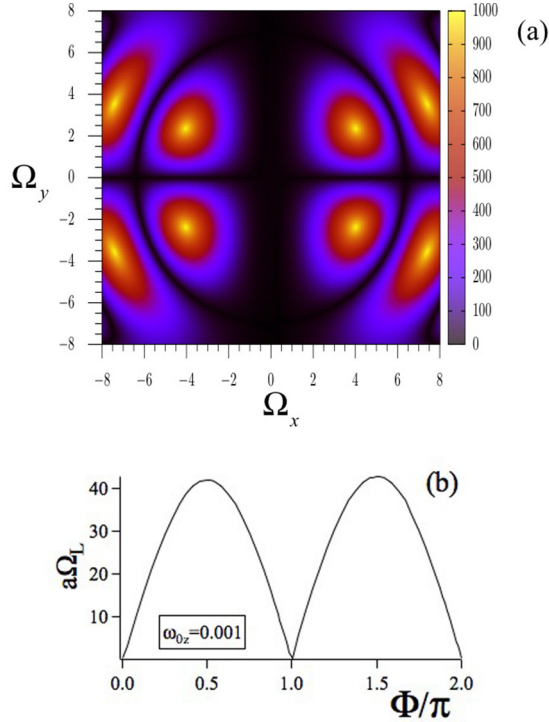
FIG. 7. In (a) numerical results for $a\Omega_L$ in the 2D (Ω_x, Ω_y) plane at $\omega_{0z} = 0.001$, $\omega_{0x} = \omega_{0y} = 0$, $p = 3$, and $\Phi = \pi/2$. The $\simeq 1000$ maximum value is reached at ($\Omega_x \simeq \pm 3.9$, $\Omega_y \simeq \pm 2.4$) and ($\Omega_x \simeq \pm 7.5$, $\Omega_y \simeq \pm 3.6$) values. In (b) from the perturbation treatment, $a\Omega_L$ vs Φ derived at $p = 3$, $\omega_{0z} = 0.001$, $\Omega_x = 3.9$, $\Omega_y = 1$, with maximum ≈ 43.

for dressing parameters close to a transition from one real and two complex conjugates to three real ones, as those plotted in Fig. 4(c). The four-times increase produced by the dual-dressing increase is certainly useful in experiments such as that quoted above. The effective negative sign of the effective Landé g factor should be no problem for the experimentalists. In an experimental implementation, because the remaining **g**-tensor principal values remain around one or below, the

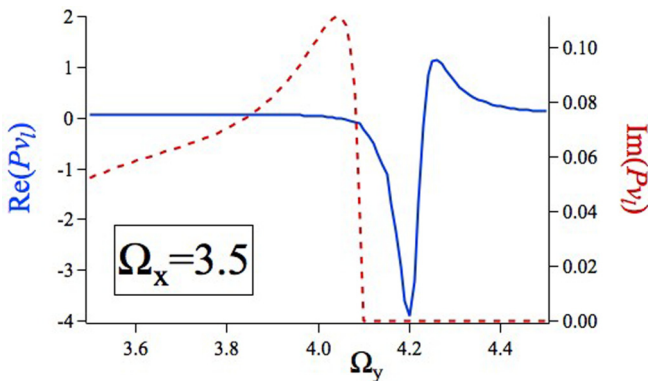FIG. 8. Numerical results for Pv_l, the largest principal value of the **g** tensor, vs Ω_y, for $\Omega_x = 3.5$, $p = 1$, and $\Phi = \pi/2$. Real Re(Pv_l) and complex Im(Pv_l) parts are plotted. The Ω_y parameter is varied in the transition region from one real and two complex principal values to three real values. Notice that the largest absolute Re(Pv_l) value is negative.

dressing fields should be oriented in space in order to align the principal axis of interest with the experimentally applied Stern-Gerlach magnetic gradient.

B. Magnetic field compensation

We target here the compensation of a static field arbitrarily oriented in space by generating an opposite sign synthetic magnetic field. Three-dimensional (3D) compensation is expressed by the following expression:

$$\Omega_L = 0, \tag{47}$$

or equivalently,

$$h_x = h_y = h_z = 0. \tag{48}$$

Instead, for one or two dimensions (1D or 2D) we impose $h_i = 0$ for the required dimensions. Compensations of 3D and 2D magnetic fields are required in high-resolution experiments. For instance, in interferometric investigations with artificial or natural atoms as in [65,66], the fine tuning of the magnetic response with a controlled compensation on different spatial directions produces a higher precision.

Nearly periodic zero values of the Larmor frequency appear in Figs. 2 and 7(a). From the $h_s^{(1)}$, $\mathbf{g}^{(1)}$ expressions of Eqs. (30) and (31) we derive that the applications of dressing fields along the three spatial directions produce the compensation of an arbitrary magnetic field configuration. However, the action of several strong dressings cannot be handled by a perturbation approach, and numerical solutions are required.

A more ambitious goal, denoted as second-order magic compensation or a magic shield, is to produce a reduced sensitivity to fluctuations of the dressing field or of the magnetic field, respectively [36,37,67–71]. These magic solutions are obtained by solving Eq. (48) and simultaneously imposing zero values for their derivatives with respect to the compensation parameter(s). Second-order magic dressing requires a nonlinear dependence on the control parameters, for instance, through the Bessel functions for the dressing Rabi frequencies. Nonlinear dependencies on the static magnetic fields appear at the second- and higher-order perturbation treatments.

We derive here the dressing parameters realizing a 2D magic compensation for the ^{87}Rb atomic chip studies of Refs. [72,73] for an applied 300-μT field. There the target was to reduce the transverse fields from the 0.3-μT range into the nT one. For such 2D compensation, an Ω_x dressing field is applied parallel to the noncompensated ω_{0x} field. Within the first-order perturbation treatment we derive that an $h_z^{(1)} = 0$ effective synthetic field is produced by a properly chosen $\Omega_{y5} \cos(5\tau + \pi/2)$ driving. Instead, $h_y^{(1)} = 0$ is reached, adding a properly chosen $\Omega_{y6} \cos(6\tau)$ dressing, these high harmonics being useful for the Ω_x magic compensation. Up to the second-order perturbation level the 2D compensation is given by

$$h_y = J_6(\Omega_x)\Omega_{y6} + J_0(\Omega_x)\omega_{0y}$$
$$+ \tfrac{1}{2}Q_{yx}(\Omega_x)\Omega_{y6}\omega_{0x} + 2q_s(\Omega_x)\omega_{0x}\omega_{0y} = 0,$$
$$h_z = J_5(\Omega_x)\Omega_{y5} + J_0(\Omega_x)\omega_{0z}$$
$$+ \tfrac{1}{2}Q_{zx}(\Omega_x)\Omega_{y5}\omega_{0x} + 2q_s(\Omega_x)\omega_{0x}\omega_{0z} = 0. \tag{49}$$
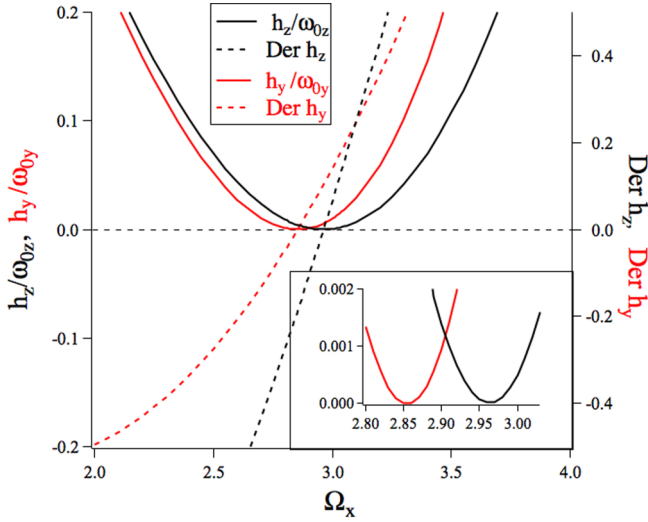
FIG. 9. On the left scale, compensation results for the h_y, h_z effective transverse magnetic fields vs the strong Ω_x dressing field in a $\omega_{0x} = 0.1$, $\omega_{0y} = \omega_{0z} = 1 \times 10^{-4}$ configuration, with weak dressing fields $\Omega_{z5} = 0.6 \times 10^{-5}$, $\Omega_{y6} = 2.4 \times 10^{-5}$. The plot of the normalized h_y/ω_{0y}, h_z/ω_{0z} ratios evidences the magic compensations. On the right scale the $\partial h_y/\partial \Omega_x$, $\partial h_z/\partial \Omega_x$ derivatives vs Ω_x in the second-order magic compensation search. Even if the null derivatives are not exactly coincident for the magic compensation, the sensitivity to the strong dressing fluctuations is reduced by three orders of magnitude. This appears in the inset plot for the normalized effective fields in the Ω_d (2.87,2.92) range.

The second-order contributions to these effective fields are greatly reduced by choosing a large dressing frequency, for instance, 30 times greater than the bare Larmor frequency, i.e., $\omega_{0x} = 0.1$. The above equations contain a nonlinear dependence on the Ω_x dressing field and therefore allow a magic compensation for that parameter, as presented in Fig. 9. The above equations, not containing a nonlinear dependence on the $(\omega_{0y}, \omega_{0z})$ parameters, do not support transverse field magic fluctuation shields. For those parameters as well for the $(\Omega_{y5}, \Omega_{y6})$ ones, magic compensations can be determined by numerical analyses. Multiple harmonic driving produces interesting compensation schemes to be explored.

C. Inhomogeneous dressing

A spatial gradient of the dressing field can increase the forces on the spins using an inhomogeneous oscillating field as for trapped ions in [74,75] and as for the Cs experiments [21,76], where we tested the dual dressing. Therefore the magnetometry applications with Ω_L deliberately spatially dependent can be enlarged by the dual-dressing configuration. Such a spatial distribution is more easily realized by operating on the position dependence of a weak-field tuning the dressing of the strong one. The atomic trapping with spatially inhomogeneous radio frequency potentials, reviewed in [77], can produce a new spatial configuration by replacing the single dressing by the dual one.

VI. CONCLUSION AND OUTLOOK

For a spin one-half system in the presence of an arbitrary static magnetic field, we study the dual dressing by a primary field and a secondary one oscillating at a harmonic frequency. Within a perturbative treatment the secondary field acts as a tuning of the first strong dressing. The two fields play an equivalent role in numerical analyses. The dual dressing introduces a very rich dynamics into a quantum system. The standard spin Larmor precession around the external static field is replaced by a dressed Larmor precession whose frequency is controlled by the dressing fields. We present dressing parameters where that frequency is, under the proper conditions, either increased 1000 times or decreased down to zero. These conditions are reached in experiments operating with nT static fields, applying electromagnetic fields whose frequency, amplitude, and phase are accessible experimentally. In magnetic resonance, i.e., the dressing by a rotating field, a resonant field creates in the rotating frame a spin precession around the rotating field with frequency determined by the rotating field amplitude. The dual dressing extends that feature to an arbitrary spatial orientation of the spin and also leads to a precession frequency as large as the electromagnetic field frequency. In addition, our nonresonant dressing acts not only on the resonant species but on all spin species of the sample, as for the investigated two-species case.

The generalization of the dressed atom to the dual driving configuration enriches the spin control, produces features useful to several quantum control directions, and enables new quantum technology explorations. The effective or fictitious fields, providing a simple and direct access to the qubit control, represent the dual-dressing handle. The commensurable and low harmonic driving is a key component of its great impact on the spin dynamics. For an initially symmetric spin system, the triaxial response created by the dual dressing introduces a controlled anisotropy where the effective field orientation is the anisotropy helm. These characteristics apply also to a multiple harmonic dressing, as a straightforward extension of our theoretical treatment.

As for other modulated systems, the micromotion represents an essential component of the spin dynamics under dual-dressing driving. Its main component is associated to the FMR frame transformation, with an additional component produced by the kick operator. The influence of the kick operator can be neglected operating at low static field, as for all dressing experiments so far. The micromotion produces additional high-harmonic components, easily separated by performing a spectral analysis of the detected experimental signal. This spectral separation allows an employ of the micromotion components to enhance the fidelities of quantum gates based on dual-dressed qubits, as performed for the trapped ions qubits; see [78] and references therein.

We have presented several dual-dressing applications in spectroscopy, atomic physics, quantum simulation, and computation. For spectroscopy, the controlled increase of the Larmor frequency shifts the spin detection towards higher frequencies where the experimental sensitivity is larger. On the opposite direction, in atomic physics experiments as atom chips or atomic interferometers the externally applied magnetic field should be compensated in order to improve the experimental precision. Under the combined action of even and odd harmonics in the secondary dressing field, the synthetic field drastically reduces the magnetic splittings in all chosen directions.

For spintronics, the dual dressing can be applied to artificial atoms, where the energy splittings produced by the solid host are equivalent to static magnetic fields considered here. Our scheme leads to a control of those energy splittings to be increased or compensated. A wide range of g-factor anisotropies appears in solid-state physics, from less than 1% in nitrogen-vacancy color centers for precision magnetic sensors [79–81] to up to 30% in InSb quantum wells for topological quantum computing [82]. The bichromatic dressing can be used either to compensate the Landé g-factor anisotropy for higher precision magnetic sensors or to increase the anisotropy and therefore the topological importance of the material.

The results of our perturbative and numerical treatments evidence the presence of symmetries for the eigenvalues and the effective and/or synthetic fields. These symmetries depend on the harmonic order and dressing phase. In [83] the group theory of the dynamical symmetries in periodic Floquet systems is applied to the nonlinear harmonic generation. Those group operations, as rotations, reflection, and different symmetries, as inversion, spatio-temporal or spatial only, should be used to analyze the response of a dual-dressed spin for a wider parameter range.

Owing to the easy experimental implementation of the double dressing, the introduction of another handle, such as the time dependence of the dressing field amplitudes, with properly designed adiabatic or superadiabatic temporal evolutions, can be used to produce new quantum superposition states. On a different direction, the application of a sinusoidal modulation to the dressing fields can open new directions for the dynamical driving of ultracold atoms in optical lattices.

The attention is here focused on qubit systems with negligible relaxation processes, as in the experiment of Ref. [21] and similar ones in ultracold atoms. It will be interesting to investigate the dual-dressing features also in the presence of relaxation processes, where Ref. [84] has proven the existence of a periodic steady state independent of the initial conditions.

APPENDIX A: NUMERICAL SOLUTION

The numerical solution of the Λ Floquet matrix requires the propagation of the operator $U(\tau)$ from $\tau = 0$ to $\tau = 2\pi$, then the diagonalization of $U(2\pi) = e^{-i\,2\pi\,\Lambda}$ [2], leading to

$$U(2\pi)|\lambda_\pm\rangle = e^{-12\pi\lambda_\pm}|\lambda_\pm\rangle, \tag{A1}$$

with $\lambda_\pm$ eigenvalues and the Floquet Λ matrix

$$\Lambda = \sum_{j=\pm} \lambda_j |\lambda_j\rangle\langle\lambda_j|. \tag{A2}$$

The components of the vector $\boldsymbol{h}$ are obtained as

$$h_j = \text{trace}(\Lambda\sigma_j), \quad j = x, y, z. \tag{A3}$$

APPENDIX B: FMR FLOQUET-MAGNUS EXPANSION

The Magnus expansion writes in an exponential form the time evolution operator of a linear system [85]. When applied to the FMR U_I time evolution operator of Eq. (13) under a generic H_I Hamiltonian,

$$i\dot{U}_I(\tau) = H_I(\tau)\,U_I(\tau), \tag{B1}$$

it parametrizes the operator as

$$U_I(\tau) = e^{-iW(\tau)}. \tag{B2}$$

This leads to, for the $W(\tau)$ exponent,

$$\dot{W}(\tau) = H_I(\tau) + \frac{i}{2}[W(\tau), H_I(\tau)] + \cdots. \tag{B3}$$

If $H_I(\tau)$ is "small," i.e., $H_I \to \epsilon H_I$ for a small ϵ, expressing $W = \epsilon W_1 + \epsilon^2 W_2 + \cdots$ one finds for the first terms

$$W_1(\tau) = \int_0^\tau H_I(\tau_1)\,d\tau_1,$$

$$W_2(\tau) = \frac{-i}{2}\int_0^\tau d\tau_1\,[H_I(\tau_1), W_1(\tau_1)]. \tag{B4}$$

Within the Fourier description of Eq. (17), the Magnus expansion is applied to the $\mathcal{K}$ and Λ exponents. Letting $H \to \epsilon H$ as above, we write $\mathcal{K}(\tau) = \epsilon\mathcal{K}_1(\tau) + \epsilon^2\mathcal{K}_2(\tau)\ldots$ and $\Lambda = \epsilon\Lambda_1 + \epsilon^2\Lambda_2 + \cdots$. Thus the following formulas are obtained:

$$\Lambda_1 = \frac{1}{2\pi}\int_0^{2\pi} H_I(\tau)d\tau,$$

$$\mathcal{K}_1(\tau) = \int_0^\tau H_I(\tau')d\tau' - \tau\Lambda_1,$$

$$\Lambda_2 = -\frac{i}{4\pi}\int_0^{2\pi}[H_I(\tau) + \Lambda_1, \mathcal{K}_1(\tau)]d\tau,$$

$$\mathcal{K}_2(\tau) = -\tau\Lambda_2 - \frac{i}{4\pi}\int_0^\tau[H_I(\tau') + \Lambda_1, \mathcal{K}_1(\tau')]d\tau'. \tag{B5}$$

APPENDIX C: FOURIER EXPANSIONS OF THE DRIVING

In order to simplify the mathematical derivations, we introduce a few time-dependent functions. For a generic accumulated phase introduced by Eq. (12), more general than the sinusoidal one, we define the functions ($c_0 = \cos\varphi_x$, $s_0 = \sin\varphi_x$), ($c_1 = s_y\cos\varphi_x$, $s_1 = s_y\sin\varphi_x$, and (α_n, β_n), given by

$$e^{i\varphi_x(\tau)} \equiv c_0(\tau) + i\,s_0(\tau) = \sum_{n=-\infty}^{+\infty} \alpha_n e^{in\tau},$$

$$s_y(\tau)e^{i\varphi_x(\tau)} \equiv c_1(\tau) + i\,s_1(\tau) = \sum_{n=-\infty}^{+\infty} \beta_n e^{in\tau}. \tag{C1}$$

From the α_n definition, $|\alpha_0| \leqslant 1$ is easily derived.

In addition we introduce $C_i(\tau)$, $S_i(\tau)$ as the primitives of the lower case functions, respectively, as

$$\int_0^\tau e^{i\varphi_x(\tau')}d\tau' \equiv C_0(\tau) + i\,S_0(\tau)$$

$$= \alpha_0\tau - i\sum_{n\neq 0}\alpha_n\frac{e^{in\tau} - 1}{n}, \tag{C2a}$$

$$\int_0^\tau s_y(\tau')e^{i\varphi_x(\tau')}d\tau' \equiv C_1(\tau) + i S_1(\tau)$$

$$= \beta_0\tau - i\sum_{n\neq 0}\beta_n \frac{e^{in\tau} - 1}{n}. \qquad \text{(C2b)}$$

Explicitly we obtain

$$C_0 = \text{Re}(\alpha_0)\tau + \sum_{n\geqslant 1}\left[\frac{\text{Im}(\alpha_n - \alpha_{-n})}{n}(\cos(n\tau) - 1)\right.$$

$$\left. + \frac{\text{Re}(\alpha_n + \alpha_{-n})}{n}\sin(n\tau)\right], \qquad \text{(C3)}$$

$$S_0 = \text{Im}(\alpha_0)\tau + \sum_{n\geqslant 1}\left[\frac{-\text{Re}(\alpha_n + \alpha_{-n})}{n}(\cos(n\tau) - 1)\right.$$

$$\left. + \frac{\text{Im}(\alpha_n - \alpha_{-n})}{n}\sin(n\tau)\right], \qquad \text{(C4)}$$

and a similar expression for C_1 and S_1, replacing α_n by β_n.

For the cosine signal drivings of Eq. (2) and the sinusoidal accumulated phase of Eq. (12) we obtain

$$e^{i\varphi_x(\tau)} = \cos(\varphi_x(\tau)) + i\sin(\varphi_x(\tau)) = \sum_n J_n(\Omega_x)e^{in\tau}, \qquad \text{(C5)}$$

where J_n are the Bessel functions of first kind. Therefore the α_n and β_n functions become

$$\alpha_n = J_n(\Omega_x),$$
$$\beta_n = \tfrac{1}{2}(e^{i\Phi}J_{n-p}(\Omega_x) + e^{-i\Phi}J_{n+p}(\Omega_x)). \qquad \text{(C6)}$$

The c_0 and s_0 functions become

$$c_0(\tau) = J_0(\Omega_x) + 2\sum_{n\geqslant 1}J_{2n}(\Omega_x)\cos(2n\tau), \qquad \text{(C7)}$$

$$s_0(\tau) = 2\sum_{n\geqslant 0}J_{2n+1}(\Omega_x)\sin[(2n+1)\tau], \qquad \text{(C8)}$$

and the c_1 and s_1 functions become

$$2c_1(\tau) = \cos\Phi(J_{-p} + J_p) + \sum_{n\geqslant 1}[-\sin\Phi(J_{n-p} - J_{-n-p} - J_{n+p} + J_{-n+p})\sin(n\tau)$$

$$+ \cos\Phi(J_{n-p} + J_{-n-p} + J_{n+p} + J_{-n+p})\cos(n\tau)],$$

$$2s_1(\tau) = \sin\Phi(J_{-p} - J_p)x + \sum_{n\geqslant 1}[\cos\Phi(J_{n-p} - J_{-n-p} + J_{n+p} - J_{-n+p})\sin(n\tau)$$

$$+ \sin\Phi(J_{n-p} - J_{-n-p} - J_{n+p} + J_{-n+p})\cos(n\tau)], \qquad \text{(C9)}$$

where, here and also in the following, all the Bessel functions are calculated at the Ω_x value. The primitive functions then become

$$C_0(\tau) = J_0\tau + \sum_{n\geqslant 1}(J_{2n}/n)\sin(2n\tau),$$

$$S_0(\tau) = 2\sum_{n\geqslant 0}(J_{2n+1}/(2n+1))(1 - \cos[(2n+1)\tau],$$

$$2C_1(\tau) = \cos\Phi(J_{-p} + J_p)\tau + \sum_{n\geqslant 1}\left[\sin\Phi\frac{J_{n-p} - J_{-n-p} - J_{n+p} + J_{-n+p}}{n}[\cos(n\tau) - 1)]\right.$$

$$\left. + \cos\Phi\frac{J_{n-p} + J_{-n-p} + J_{n+p} + J_{-n+p}}{n}\sin(n\tau)\right],$$

$$2S_1(\tau) = \sin\Phi(J_{-p} - J_p)\tau + \sum_{n\geqslant 1}\left[-\cos\Phi\frac{J_{n-p} - J_{-n-p} + J_{n+p} - J_{-n+p}}{n}[\cos(n\tau) - 1)]\right.$$

$$\left. + \sin\Phi\frac{J_{n-p} - J_{-n-p} - J_{n+p} + J_{-n+p}}{n}\sin(n\tau)\right]. \qquad \text{(C10)}$$

APPENDIX D: FMR EFFECTIVE FIELDS

To handle the Ω_x dressing through the FMR gauge transformation, we examine here the action of $\Omega_y s_y(t)$ and $\boldsymbol{\omega}_0$ on the spin evolution, applying the Magnus perturbation approach. Using the functions defined by Eqs. (C1), we write the $\boldsymbol{h}^{\text{FMR}}$ of Eq. (16) as

$$\boldsymbol{h}^{\text{FMR}}(\tau) = \Omega_y\begin{pmatrix} 0 \\ c_1 \\ -s_1 \end{pmatrix} + \begin{pmatrix} 1 & 0 & 0 \\ 0 & c_0 & s_0 \\ 0 & -s_0 & c_0 \end{pmatrix}\begin{pmatrix} \omega_{0x} \\ \omega_{0y} \\ \omega_{0z} \end{pmatrix}$$

$$= \boldsymbol{h}_0^{\text{FMR}}(\tau) + \mathbf{g}_0(\tau)\boldsymbol{\omega}_0, \qquad \text{(D1)}$$

with the 3×3 $\mathbf{g}_0(\tau)$ matrix determining the static field contribution in analogy to the effective field perturbation expansion.

We define the $\boldsymbol{H}^{\text{FMR}}$ vector as definite integral of $\boldsymbol{h}^{\text{FMR}}$:

$$\boldsymbol{H}^{\text{FMR}}(\tau) = \int_0^\tau \boldsymbol{h}^{\text{FMR}}(\tau')d\tau'. \qquad \text{(D2)}$$

For the $\boldsymbol{h}^{\text{FMR}}(\tau)$ and $\boldsymbol{H}^{\text{FMR}}(\tau)$ quantities, also the mean values over the $(0, 2\pi)$ interval are required and denoted in the following as $\langle\boldsymbol{h}^{\text{FMR}}\rangle$ and $\langle\boldsymbol{H}^{\text{FMR}}\rangle$, respectively. Notice

$$\boldsymbol{H}^{\text{FMR}}(2\pi) = 2\pi\langle\boldsymbol{h}^{\text{FMR}}\rangle, \qquad \text{(D3)}$$

and the following connection between mean values:

$$\langle \tau \boldsymbol{h}^{\text{FMR}} \rangle = 2\pi \langle \boldsymbol{h}^{\text{FMR}} \rangle - \langle \boldsymbol{H}^{\text{FMR}} \rangle. \quad \text{(D4)}$$

Similarly for $\boldsymbol{H}^{\text{FMR}}(\tau)$, using the functions of Eqs. (C2) we write

$$\boldsymbol{H}^{\text{FMR}}(\tau) = \Omega_y \begin{pmatrix} 0 \\ C_1 \\ -S_1 \end{pmatrix} + \begin{pmatrix} \tau & 0 & 0 \\ 0 & C_0 & S_0 \\ 0 & -S_0 & C_0 \end{pmatrix} \begin{pmatrix} \omega_{0x} \\ \omega_{0y} \\ \omega_{0z} \end{pmatrix}$$

$$= \boldsymbol{H}_0^{\text{FMR}}(\tau) + \mathbf{G}_0(\tau)\boldsymbol{\omega}_0, \quad \text{(D5)}$$

again with the $\mathbf{G}_0(\tau)$ 3×3 matrix characterizing the static field dependence.

Replacing the above FMR quantities within the Fourier-Magnus expansions of Eqs. (B5), we find

$$\Lambda_1 = \frac{1}{2} \langle \boldsymbol{h}^{\text{FMR}} \rangle \cdot \boldsymbol{\sigma}, \quad \text{(D6)}$$

$$\mathcal{K}_1(\tau) = \left[\frac{1}{2} \int_0^\tau \boldsymbol{h}^{\text{FMR}}(\tau') d\tau' - \tau \frac{1}{2} \langle \boldsymbol{h}^{\text{FMR}} \rangle \right] \cdot \boldsymbol{\sigma}$$

$$= \frac{1}{2} [\boldsymbol{H}^{\text{FMR}}(\tau) - \tau \langle \boldsymbol{h}^{\text{FMR}} \rangle] \cdot \boldsymbol{\sigma}. \quad \text{(D7)}$$

Replacing these quantities within the Λ_2 expression of Eqs. (B5) and using Eqs. (D3) and (D4), the second-order correction results in

$$\Lambda_2 = \tfrac{1}{4} \langle \boldsymbol{h}^{\text{FMR}} \times \boldsymbol{H}^{\text{FMR}} \rangle \cdot \boldsymbol{\sigma}. \quad \text{(D8)}$$

From the above Λ_1 and Λ_2 expressions, the first- and second-order effective fields of Eq. (18) result in

$$\boldsymbol{h} \approx \boldsymbol{h}^{(1)} + \boldsymbol{h}^{(2)} = \langle \boldsymbol{h}^{\text{FMR}} \rangle + \tfrac{1}{2} \langle \boldsymbol{h}^{\text{FMR}} \times \boldsymbol{H}^{\text{FMR}} \rangle. \quad \text{(D9)}$$

Using the expressions of Eqs. (D1) and (D5) and performing some algebra, the second-order contribution is rewritten as

$$\boldsymbol{h}^{(2)} = \tfrac{1}{2} \langle \boldsymbol{h}_0^{\text{FMR}} \times \boldsymbol{H}_0^{\text{FMR}} \rangle$$

$$+ \tfrac{1}{2} \left(\langle \boldsymbol{h}_0^{\text{FMR}} \times [\mathbf{G}_0\boldsymbol{\omega}_0] \rangle - \langle \boldsymbol{H}_0^{\text{FMR}} \times [\mathbf{g}_0\boldsymbol{\omega}_0] \rangle \right)$$

$$+ \tfrac{1}{2} \langle [\mathbf{g}_0\boldsymbol{\omega}_0] \times [\mathbf{G}_0\boldsymbol{\omega}_0] \rangle, \quad \text{(D10)}$$

where the three lines give the contributions of Eqs. (21), (23), and (25), respectively.

APPENDIX E: COSINE SECOND-ORDER PERTURBATION

The Q_x amplitude of the synthetic field $\boldsymbol{h}_{s,x}^{(2)}$ is derived from Eq. (22), inserting the cosine driving β_n expressions of Eqs. (C6):

$$Q_x = -\frac{J_p}{2} [1 + (-1)^p \cos(2\Phi)] \sum_{n \geqslant 1} \frac{J_{n+p} - J_{p-n}}{n}$$

$$- \frac{J_p}{2} [(-1)^p + \cos(2\Phi)] \sum_{n \geqslant 1} \frac{J_{n-p} - J_{-p-n}}{n}. \quad \text{(E1)}$$

For the $\mathbf{g}^{(2)}$ tensor components of Eq. (23), by inserting the α_n and β_n expressions quoted above one finds

$$\begin{aligned} Q_{xy} &= (A+B)\cos(\Phi), \\ Q_{xz} &= -(A-B)\sin(\Phi), \\ Q_{yx} &= C\cos(\Phi), \\ Q_{zx} &= -D\sin(\Phi), \end{aligned} \quad \text{(E2)}$$

where

$$A = \sum_{n \neq 0} \frac{1}{n} (J_{n-p}J_n - J_nJ_{-p} - J_0J_{n-p}),$$

$$B = \sum_{n \neq 0} \frac{1}{n} (J_{n+p}J_n - J_nJ_p - J_0J_{n+p}),$$

$$C = \sum_{n \geqslant 1} \frac{1}{n} (J_{p+n} - J_{p-n} + J_{n-p} - J_{-n-p}),$$

$$D = \sum_{n \geqslant 1} \frac{1}{n} (J_{-p+n} - J_{-p-n} - J_{n+p} + J_{p-n}). \quad \text{(E3)}$$

Finally, from the (α_n, β_n) Bessel function dependencies we obtain for the $\mathbf{f}^{(2)}$ components of Eqs. (26),

$$q_c = 0,$$

$$q_s = \sum_{n=0}^{+\infty} \frac{J_{2n+1}}{2n+1},$$

$$q_0 = -J_0 q_s. \quad \text{(E4)}$$

APPENDIX F: KICK OPERATOR

The kick operator $\mathcal{K}_1$ given in Eq. (D7) at the first perturbation order is rewritten, inserting Eq. (D5) for the $\boldsymbol{H}^{\text{FMR}}$ vector and deriving $\langle \boldsymbol{h}^{\text{FMR}} \rangle$ from Eq. (D1). It leads to

$$\mathcal{K}_1(\tau) = \frac{\Omega_y}{2} \begin{pmatrix} 0 \\ \tilde{C}_1 \\ -\tilde{S}_1 \end{pmatrix} \cdot \boldsymbol{\sigma} + \frac{1}{2} \begin{pmatrix} 0 & 0 & 0 \\ 0 & \tilde{C}_0 & \tilde{S}_0 \\ 0 & -\tilde{S}_0 & \tilde{C}_0 \end{pmatrix} \begin{pmatrix} \omega_{0x} \\ \omega_{0y} \\ \omega_{0z} \end{pmatrix} \cdot \boldsymbol{\sigma},$$

$$\text{(F1)}$$

where for the cosine driving the following combined $(\tilde{C}_i, \tilde{S}_i)$ functions are introduced:

$$\tilde{C}_0(\tau) = \sum_{n \geqslant 1} (J_{2n}/n) \sin(2n\tau),$$

$$\tilde{S}_0(\tau) = 2 \sum_{n \geqslant 0} (J_{2n+1}/(2n+1))[1 - \cos((2n+1)\tau)],$$

$$\tilde{C}_1(\tau) = C_1 - \tau \langle c_1 \rangle = C_1 - \tau \text{Re}(\beta_0),$$

$$\tilde{S}_1(\tau) = S_1 - \tau \langle s_1 \rangle = S_1 - \tau \text{Im}(\beta_0), \quad \text{(F2)}$$

and

$$\beta_0 = \cos(\Phi)(J_p + J_{-p}) - i\sin(\Phi)(J_p - J_{-p}). \quad \text{(F3)}$$

For the class of single cosine dressing experiments, as for the original one by Landré *et al.* [7] where $\Omega_y = 0$ and $\omega_{0x} = \omega_{0z} = 0$, the above kick operator reduces to

$$\mathcal{K}_1(\tau) = \tfrac{1}{2} \omega_{0y} (\tilde{C}_0 \sigma_y - \tilde{S}_0 \sigma_z). \quad \text{(F4)}$$

For the Cs dual-cosine-dressing experiment of [21] where $\omega_{0y} = 0$, the above kick operator reduces to

$$\mathcal{K}_1(\tau) = \frac{\Omega_y}{2} (\tilde{C}_1 \sigma_y - \tilde{S}_1 \sigma_z) + \frac{\omega_{0z}}{2} (\tilde{S}_0 \sigma_y + \tilde{C}_0 \sigma_z). \quad \text{(F5)}$$

For all these experiments operating with low Ω_y and $\boldsymbol{\omega}_0$ values, the spin micromotion of Eq. (36) is dominated by the first term due to the transformation to the FMR frame.

[1] N. Goldman and J. Dalibard, Phys. Rev. X **4**, 031027 (2014).

[2] M. Bukov, L. D'Alessio, and A. Polkovnikov, Adv. Phys. **64**, 139 (2015).

[3] A. Eckardt, Rev. Mod. Phys. **89**, 011004 (2017).

[4] C. Cohen-Tannoudji and S. Haroche, C. R. Acad. Sci. Paris B **262**, 268 (1966).

[5] S. Haroche, C. Cohen-Tannoudji, C. Audoin, and J. P. Schermann, Phys. Rev. Lett. **24**, 861 (1970).

[6] S. Haroche and C. Cohen-Tannoudji, Phys. Rev. Lett. **24**, 974 (1970).

[7] C. C. Landré, C. Cohen-Tannoudji, J. Dupont-Roc, and S. Haroche, J. Physique **31**, 971 (1970).

[8] E. Muskat, D. Dubbers, and O. Schärpf, Phys. Rev. Lett. **58**, 2047 (1987).

[9] R. Golub and S. K. Lamoreaux, Phys. Rep. **237**, 1 (1994).

[10] T. Ito, N. Shimomura, and T. Yabuzaki, J. Phys. Soc. Jpn. **72**, 1302 (2003).

[11] A. Esler, J. C. Peng, D. Chandler, D. Howell, S. K. Lamoreaux, C. Y. Liu, and J. R. Torgerson, Phys. Rev. C **76**, 051302(R) (2007).

[12] P.-H. Chu, A. M. Esler, J. C. Peng, D. H. Beck, D. E. Chandler, S. Clayton, B.-Z. Hu, S. Y. Ngan, C. H. Sham, L. H. So, S. Williamson, and J. Yoder, Phys. Rev. C **84**, 022501(R) (2011).

[13] G. Bevilacqua, V. Biancalana, Y. Dancheva, and L. Moi, Phys. Rev. A **85**, 042510 (2012).

[14] F. Gerbier, A. Widera, S. Fölling, O. Mandel, and I. Bloch, Phys. Rev. A **73**, 041602(R) (2006).

[15] S. Hofferberth, B. Fischer, T. Schumm, J. Schmiedmayer, and I. Lesanovsky, Phys. Rev. A **76**, 013401 (2007).

[16] Q. Beaufils, T. Zanon, R. Chicireanu, B. Laburthe-Tolra, E. Maréchal, L. Vernac, J.-C. Keller, and O. Gorceix, Phys. Rev. A **78**, 051603(R) (2008).

[17] A. A. Pervishko, O. V. Kibis, S. Morina, and I. A. Shelykh, Phys. Rev. B **92**, 205403 (2015).

[18] C. M. Swank, E. K. Webb, X. Liu, and B. W. Filippone, Phys. Rev. A **98**, 053414 (2018).

[19] C.-P. Hao, Z.-R. Qiu, Q. Sun, Y. Zhu, and D. Sheng, Phys. Rev. A **99**, 053417 (2019).

[20] M. Grifoni and P. Hänggi, Phys. Rep. **304**, 229 (1998).

[21] G. Bevilacqua, V. Biancalana, A. Vigilante, T. Zanon-Willette, and E. Arimondo, Phys. Rev. Lett. **125**, 093203 (2020).

[22] J. H. Shirley, Phys. Rev. **138**, B979 (1965).

[23] N. Nayak and G. S. Agarwal, Phys. Rev. A **31**, 3175 (1985).

[24] T.-S. Ho, S.-I. Chu, and J. V. Tietz, Chem. Phys. Lett. **96**, 464 (1983).

[25] S.-I. Chu, in *Advances in Atomic and Molecular Physics*, edited by D. Bates and B. Bederson (Academic Press, New York, 1985), Vol. 21, pp. 197–253.

[26] A. N. Poertner and J. D. D. Martin, Phys. Rev. A **101**, 032116 (2020).

[27] M. Leskes, P. K. Madhu, and S. Vega, Prog. Nucl. Magn. Reson. Spectrosc. **57**, 345 (2010).

[28] Z. Ficek and H. S. Freedhoff, in *Progress in Optics*, edited by E. Wolf (Elsevier, New York, 2000), Vol. 40, pp. 389–441.

[29] M. P. Silveri, J. A. Tuorila, E. V. Thuneberg, and G. S. Paraoanu, Rep. Prog. Phys. **80**, 056002 (2017).

[30] M. Peiris, K. Konthasinghe, Y. Yu, Z. C. Niu, and A. Muller, Phys. Rev. B **89**, 155305 (2014).

[31] A. M. Satanin, M. V. Denisenko, A. I. Gelman, and F. Nori, Phys. Rev. B **90**, 104516 (2014).

[32] F. Forster, M. Mühlbacher, R. Blattmann, D. Schuh, W. Wegscheider, S. Ludwig, and S. Kohler, Phys. Rev. B **92**, 245422 (2015).

[33] J. Pan, H. Z. Jooya, G. Sun, Y. Fan, P. Wu, D. A. Telnov, S.-I. Chu, and S. Han, Phys. Rev. B **96**, 174518 (2017).

[34] K. Dai, H. Wu, P. Zhao, M. Li, Q. Liu, G. Xue, X. Tan, H. Yu, and Y. Yu, Appl. Phys. Lett. **111**, 242601 (2017).

[35] C. L. Garrido Alzar, H. Perrin, B. M. Garraway, and V. Lorent, Phys. Rev. A **74**, 053413 (2006).

[36] D. Trypogeorgos, A. Valdés-Curiel, N. Lundblad, and I. B. Spielman, Phys. Rev. A **97**, 013407 (2018).

[37] N. Aharon, N. Spethmann, I. D. Leroux, P. O. Schmidt, and A. Retzker, New J. Phys. **21**, 083040 (2019).

[38] K. Luksch, E. Bentine, A. J. Barker, S. Sunami, T. L. Harte, B. Yuen, and C. J. Foot, New J. Phys. **21**, 073067 (2019).

[39] T. Yabuzaki, S. Nakayama, Y. Murakami, and T. Ogawa, Phys. Rev. A **10**, 1955 (1974).

[40] N. Tsukada, T. Nakayama, S. Ibuki, T. Akiba, and K. Tomishima, Phys. Rev. A **23**, 1855 (1981).

[41] X.-T. Lu, T. Wang, T. Li, C.-H. Zhou, M.-J. Yin, Y.-B. Wang, X.-F. Zhang, and H. Chang, Phys. Rev. Lett. **127**, 033601 (2021).

[42] D. Farrelly and J. A. Milligan, Phys. Rev. E **47**, R2225(R) (1993).

[43] J. Karczmarek, M. Stott, and M. Ivanov, Phys. Rev. A **60**, R4225(R) (1999).

[44] F. Görg, K. Sandholzer, J. Minguzzi, R. Desbuquois, M. Messer, and T. Esslinger, Nat. Phys. **15**, 1161 (2019).

[45] H. Zhao, J. Knolle, and F. Mintert, Phys. Rev. A **100**, 053610 (2019).

[46] K. Viebahn, J. Minguzzi, K. Sandholzer, A.-S. Walter, M. Sajnani, F. Görg, and T. Esslinger, Phys. Rev. X **11**, 011057 (2021).

[47] D. Loginov, S. A. Novikov, and L. Novikov, Opt. Spectrosc. **55**, 438 (1983).

[48] T. L. Harte, E. Bentine, K. Luksch, A. J. Barker, D. Trypogeorgos, B. Yuen, and C. J. Foot, Phys. Rev. A **97**, 013616 (2018).

[49] A. P. Saiko, S. A. Markevich, and R. Fedaruk, Phys. Rev. A **98**, 043814 (2018).

[50] I. Goychuk and P. Hänggi, Europhys. Lett. **43**, 503 (1998).

[51] V. Lebedev and F. Renzoni, Phys. Rev. A **80**, 023422 (2009).

[52] P. Hänggi and F. Marchesoni, Rev. Mod. Phys. **81**, 387 (2009).

[53] D. Witthaut, T. Salger, S. Kling, C. Grossert, and M. Weitz, Phys. Rev. A **84**, 033601 (2011).

[54] S. Kohler and T. Stauber, Eur. Phys. J. B **93**, 24 (2020).

[55] R. Desbuquois, M. Messer, F. Görg, K. Sandholzer, G. Jotzu, and T. Esslinger, Phys. Rev. A **96**, 053602 (2017).

[56] M. Arnal, G. Chatelain, C. Cabrera-Gutiérrez, A. Fortun, E. Michon, J. Billy, P. Schlagheck, and D. Guéry-Odelin, Phys. Rev. A **101**, 013619 (2020).

[57] S. R. Barone, M. A. Narcowich, and F. J. Narcowich, Phys. Rev. A **15**, 1109 (1977).

[58] P. Hannaford, D. T. Pegg, and G. W. Series, J. Phys. B: At. Mol. Phys. **6**, L222 (1973).

[59] C. CohenTannoudji and D. Guery-Odelin, *Advances in Atomic Physics: An Overview* (World Scientific, Singapore, 1994).

[60] Z. Shen, M. Hsieh, and H. Rabitz, J. Chem. Phys. **124**, 204106 (2006).

[61] Y. Sui, K. Leslie, and D. Clark, IEEE Magn. Lett. **8**, 1 (2017).

[62] D. T. Pegg and G. W. Series, J. Phys. B: At. Mol. Phys. **3**, L33 (1970).

[63] N. Goldman, J. Dalibard, M. Aidelsburger, and N. R. Cooper, Phys. Rev. A **91**, 033632 (2015).

[64] Y. Margalit, Z. Zhou, S. Machluf, D. Rohrlich, Y. Japha, and R. Folman, Science **349**, 1205 (2015).

[65] K. Ono, S. N. Shevchenko, T. Mori, S. Moriyama, and F. Nori, Phys. Rev. Lett. **122**, 207703 (2019).

[66] O. Amit, Y. Margalit, O. Dobkowski, Z. Zhou, Y. Japha, M. Zimmermann, M. A. Efremov, F. A. Narducci, E. M. Rasel, W. P. Schleich, and R. Folman, Phys. Rev. Lett. **123**, 083601 (2019).

[67] T. Zanon-Willette, E. de Clercq, and E. Arimondo, Phys. Rev. Lett. **109**, 223003 (2012).

[68] L. A. Jones, J. D. Carter, and J. D. D. Martin, Phys. Rev. A **87**, 023423 (2013).

[69] L. Sárkány, P. Weiss, H. Hattermann, and J. Fortágh, Phys. Rev. A **90**, 053416 (2014).

[70] G. A. Kazakov and T. Schumm, Phys. Rev. A **91**, 023404 (2015).

[71] D. W. Booth, J. Isaacs, and M. Saffman, Phys. Rev. A **97**, 012515 (2018).

[72] C. Lacroute, F. Reinhard, F. Ramirez-Martinez, C. Deutsch, T. Schneider, J. Reichel, and P. Rosenbusch, IEEE Trans. Ultrason. Ferroelectr, Freq. Control **57**, 106 (2010).

[73] C. Deutsch, F. Ramirez-Martinez, C. Lacroûte, F. Reinhard, T. Schneider, J. N. Fuchs, F. Piéchon, F. Laloë, J. Reichel, and P. Rosenbusch, Phys. Rev. Lett. **105**, 020401 (2010).

[74] C. Ospelkaus, C. E. Langer, J. M. Amini, K. R. Brown, D. Leibfried, and D. J. Wineland, Phys. Rev. Lett. **101**, 090502 (2008).

[75] S. Wölk and C. Wunderlich, New J. Phys. **19**, 083021 (2017).

[76] G. Bevilacqua, V. Biancalana, Y. Dancheva, and A. Vigilante, Phys. Rev. Appl. **11**, 024049 (2019).

[77] H. Perrin and B. M. Garraway, in *Advances in Atomic, Molecular and Optical Physics*, edited by E. Arimondo, C. C. Lin, and S. F. Yelin (Academic Press, New York, 2017), Vol. 66, pp. 181–262.

[78] A. K. Ratcliffe, L. M. Oberg, and J. J. Hope, Phys. Rev. A **101**, 052332 (2020).

[79] M. W. Doherty, N. Manson, P. Paul Delaney, F. Jelezko, J. Wrachtrup, and L. Hollenberg, Phys. Rep. **528**, 1 (2013).

[80] L. Rondin, J.-P. Tetienne, T. Hingant, J.-F. Roch, P. Maletinsky, and V. Jacques, Rep. Prog. Phys. **77**, 056503 (2014).

[81] R. Schirhagl, K. Chang, M. Loretz, and C. L. Degen, Annu. Rev. Phys. Chem. **65**, 83 (2014).

[82] F. Qu, J. van Veen, F. K. de Vries, A. J. A. Beukman, M. Wimmer, W. Yi, A. A. Kiselev, B.-M. Nguyen, M. Sokolich, M. J. Manfra, F. Nichele, C. M. Marcus, and L. P. Kouwenhoven, Nano Lett. **16**, 7509 (2016).

[83] O. Neufeld, D. Podolsky, and O. Cohen, Nat. Commun. **10**, 405 (2019).

[84] V. I. Yudin, A. V. Taichenachev, and M. Y. Basalaev, Phys. Rev. A **93**, 013820 (2016).

[85] S. Blanes, F. Casas, J. A. Oteo, and J. Ros, Phys. Rep. **470**, 151 (2009).